Mathematical modeling of the contour evolution of heavy plates in hot rolling

authored by **F. Schausberger, A. Steinboeck, and A. Kugi**

and published in *Applied Mathematical Modelling.*

Read more ACIN papers or get this document:

http://www.acin.tuwien.ac.at/literature

Contact:

Automation and Control Institute (ACIN)	Internet: www.acin.tuwien.ac.at
Vienna University of Technology	E-mail: office@acin.tuwien.ac.at
Gusshausstrasse 27-29/E376	Phone: +43 1 58801 37601
1040 Vienna, Austria	Fax: +43 1 58801 37699

Mathematical modeling of the contour evolution of heavy plates in hot rolling

F. Schausberger*, A. Steinboeck, A. Kugi

Automation and Control Institute, Vienna University of Technology, Gußhausstraße 27–29, 1040 Vienna, Austria

Abstract

This paper deals with modeling of the contour evolution of heavy plates in hot rolling. During the rolling process asymmetric rolling conditions, such as temperature gradients or non-homogeneous input thickness profiles, may lead to a non-rectangular plate contour. A continuum mechanics approach is employed to systematically derive the contour evolution of the plate based on the input and output thickness. The mathematical model covering deviations in two dimensions is solved using methods for plane problems in mechanics. A comparison between the simulated contour evolution and measurement data from a real rolling process indicates the good accuracy of the model. Moreover, the model can be executed within one millisecond on a standard computer which stresses its real-time capability. A short analysis of the main reasons for the generation of camber utilizing the proposed model is presented.

Keywords: Contour evolution in hot rolling, Camber modeling, Heavy plate mill, Extended biharmonic equation

1. Introduction

In steel rolling mills, slabs are rolled out to heavy plates with a certain plate thickness using reversing mill stands. The quality of the final product depends mainly on the material properties, the thickness and the shape of the plate. Common deviations from the desired shape (shape defects) are buckles and waves. The causes of such imperfections are, e.g., the thermal expansion of the work rolls [1] or a non-homogeneous run-out table cooling [2].

This work deals with unwanted geometrical deviations of the plate contour with respect to the vertical axis of the plate, known as camber (cf. Fig. 1). Camber may lead to a lowered product quality or in the worst case, even to damaged roller tables and measurement equipment behind the rolling mill.

The main reasons for the generation of camber in the considered hot rolling process can be identified as:

- Asymmetric input and/or output thickness profiles in the lateral direction of the plate.

- Spatially non-homogeneous and time-dependent variations of the temperature of the plate.

An asymmetric output thickness profile may result from non-homogeneous rolling conditions in the lateral direction during the rolling pass. The sources of these asymmetries are:

- An asymmetric input thickness profile as a consequence of the last rolling pass.

---

*Corresponding author. *Tel.:* +43 1 58801 376231, *fax:* +43 1 58801 9376231.
Email addresses: `schausberger@acin.tuwien.ac.at` (F. Schausberger), `andreas.steinboeck@tuwien.ac.at` (A. Steinboeck), `kugi@acin.tuwien.ac.at` (A. Kugi)
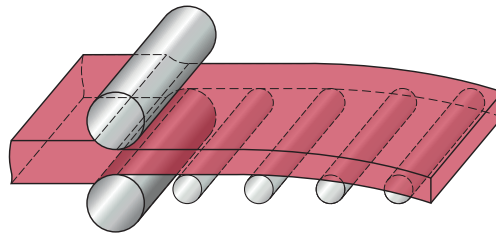
Figure 1: Sketch of the reversing mill stand and plate with camber.

- Non-homogeneous material properties (especially the resistance to deformation) due to temperature variations in the lateral direction.

- Asymmetric conditions of the mechanical setup of the rolling mill (e.g., different mill moduli on drive and operator side, asymmetric roll contours).

- An eccentric position of the plate in the rolling gap resulting from a deviation of the straight movement of the plate (snaking).

Note that the generation of camber caused by these reasons occurs during the rolling pass.

Beside the influence on the deformation properties of the plate, the temperature of the plate also causes a dilatation. Therefore, e.g., a temperature gradient in the lateral direction of the rolled plate with rectangular shape leads to a cambered plate after cooling down to a homogeneous (ambient) temperature. Because this effect occurs mainly after the rolling of the plate, it is not explicitly considered in this work.

In the past, several approaches were suggested to model the contour evolution of a plate in hot rolling and the strip movement in tandem mills. The existing models may be classified into two categories: The first ones focus on the modeling of the lateral position of the plate during the rolling pass. In heavy plate rolling, the resulting contour of the plate and its evolution are of special interest. This contour defines the usable area of the final plate. These models typically come up with a moderate computational effort. The models belonging to the second category are covering complex material properties of the rolled out plate to estimate the plate contour. These models have a high accuracy but entail large computational effort, which may render them unsuitable for real-time control.

One of the models belonging to the first category is proposed in [3]. The effect of snaking of a strip in a tandem cold rolling mill is analyzed. The model utilizes the plastic deformation of the strip as well as the elastic deformation of the rolls and the mill housing to predict the angular velocity of the strip at the entry and exit of the rolling gap. The lateral position of the strip is derived from the angular velocity vector by considering the rigid body motion of the strip outside the rolling gap.

Shiraishi et al. (cf. [4]) investigated the relation between camber and a thickness wedge of the strip under restrictions of the lateral movement of the strip. The proposed model also includes the use of edgers at the rolling gap entrance and the application of tension on the rolled strip. A model based on the conservation of mass in the rolling gap is used to compute the curvature of the strip. Experimental results are provided from a laboratory rolling mill to investigate the effects of the restrictions of the strip movement.

The effects of asymmetric rolling conditions in strip rolling were analyzed in [5]. The mill stretch and the deformation of the roll stack are used to approximate the lateral thickness profile, the resulting camber and the snaking of the strip at the exit of the rolling gap.

An early control-based camber reduction was developed in [6]. They joined three measurement devices for the lateral position of the plate located downstream of the rolling mill to determine the actual plate camber. Furthermore, the control design is based on the prediction of the curvature of the plate and the difference of the rolling gap height on the operator and drive side is used as control input.

In contrast, [7] suggests to use the bending forces applied to the roll as control inputs for a state feedback controller. The bending cylinders feature a faster dynamic response than the rolling gap

2

actuators. A state space model of the lateral position of the strip in the rolling gap including simple actuator dynamics was derived and a state observer was developed to estimate the unknown states of the system.

Kiyota et al. (cf. [8]) derived a slightly modified model based on [3]. In [8] an adjustment coefficient accounting for different rolling conditions is added. Furthermore, an optimal regulator and a state observer were designed to reduce the snaking of the strip.

Okada et al. (cf. [9]) used a sliding mode controller combined with a state observer to reduce the lateral motion of the strip. The asymmetry of the rolling gap height is used as input of the linear mathematical model.

To measure and counteract occurring camber, a vision based measurement system is presented in [10]. In particular, a CCD-camera and adequate image processing algorithms are employed to determine the curvature of the plates.

An MPC strategy based on a linearized system for controlling the lateral position of the strip was introduced in [11]. The MPC approach allows input and state constrains to be systematically considered in the control law. A very similar modeling approach for camber generation was suggested in [12]. They estimated the generation of camber in a roughing mill using the Frenet formula. The model is based on a prediction of the resulting curvature of the plate at the exit of the rolling gap. For verification of the proposed model, results from a finite element method (FEM) simulation were presented.

Models belonging to the second category are proposed, e.g., in [13], [14], [15] and [16]. A FEM simulation was used in [14] to predict the camber and the lateral movement of a hot rolled strip with an elastic-plastic material model. The camber model covers roll deflection as well as roll flattening during the rolling process and shows a good agreement with measurements from a pilot plant.

Also in [13] FEM is used to simulate the evolution of camber during hot rolling. The influence of lateral temperature variations of the plate on the resulting camber is investigated with a two-dimensional analysis. Furthermore, three-dimensional FEM simulations with elastic-plastic material properties were conducted to examine the effects of non-uniform rolling forces. Strategies for the reduction of camber across several rolling passes were also discussed.

Trull et al. (cf. [15]) developed an advanced finite element model of a plate mill to simulate the shape evolution of a rolled plate. The model includes the stretch of the mill housing, the profile of the rolls and the material properties of the plate. It is used to investigate the influence of the roll condition on the shape of the plate.

A 3D-FE model is used in [16] to predict the shape of heavy plates in hot rolling. In particular, a rigid plastic thermomechanical FEM was developed to investigate inhomogeneous plastic deformations. The evolution of uneven shapes in the longitudinal rolling process and the broadside-longitudinal rolling process were analyzed in detail.

Most of the proposed models were initially designed to simulate and to control the lateral strip position in tandem mills. Despite the fact that the rolling mill considered in this work is a reversing mill, these models provide a good basis for the following analysis. This is because most of the reported models do not take into account the interaction between the mill stands.

A mathematical model bridging the gap between the two different model categories is derived in this paper. This model predicts the contour of the plate, which is in contrast to the models from the first category. Additionally, it requires only a moderate computational effort compared to the models from the second category. It utilizes the input and output thickness of the plate as well as its input contour to predict the residual stresses and the contour of the plate after the rolling pass. Since the output thickness profile is assumed to be known, a model of the rolling gap is not needed in this work. The presented model serves as a solid basis for sensitivity studies regarding factors that influence the formation of camber. Furthermore, the high accuracy of the proposed model and its moderate computational costs make it suitable for model-based control concepts for the reduction of an existing camber.

The paper is organized as follows: In Section 2, the mathematical model of the contour evolution of the plate is presented. Simulation results from the proposed model are compared to measurement data in Section 3. The comparison shows that the contour evolution can be accurately predicted. In Section 4, the paper concludes with a short summary and an outlook on future research activities.

3

2. Modeling the evolution of the plate contour

This chapter is devoted to a mathematical model of the evolution of camber during the rolling process. As indicated in Fig. 2, a Cartesian coordinate system with coordinates x, y and z is used. In order to simplify the model, the following assumptions are made:

- The plate thickness profile $h_{in}(x, y)$ in lateral and longitudinal direction is known at least before each rolling pass.

- The profile of the rolling gap height $h_{out}(x, y)$ is also a given quantity.

- After the plate exits the rolling gap, no further plastic deformation occurs.

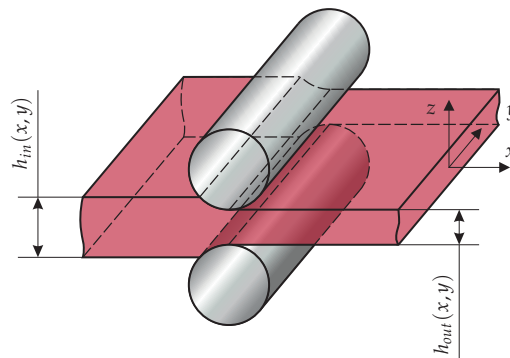- Lateral expansion in the rolling gap is not considered.

Figure 2: Plastic deformation in the rolling gap.

Knowing the thickness $h_{in}(x, y)$ of the plate before the roll pass and the thickness $h_{out}(x, y)$ at the exit of the rolling gap, the plastic strain in longitudinal direction is

$$\epsilon_{xx}^{pl} = \frac{h_{in}(x, y)}{h_{out}(x, y)} - 1, \tag{1}$$

where x and y are Lagrangian coordinates, which are valid before and after the rolling gap. The plastic strain ϵ_{xx}^{pl} is the basis for the following model.

2.1. Mathematical model for estimating camber and residual stresses

Before the first rolling pass, the plate has approximately the shape of a rectangular block. Therefore, the computational domain is initially chosen as a cuboid. As long as non-uniformities along the thickness direction of the plate are neglected, a two-dimensional problem formulation may be used. For the given problem, this simplifies the estimation of the strains and residual stresses in the plate. In the following derivation, the assumption of plane stress is made. It is motivated by the absence of surface tractions and the small dimension in thickness direction compared to the length and the width of the plate (cf. [17]). This implies that stresses along the z-direction vanish and all quantities are uniform along the z-direction.

2.1.1. Two-dimensional problem formulation

If there are no body forces, the equilibrium equations for an infinitesimal volume element in the two-dimensional space read as

$$\frac{\partial \sigma_{xx}}{\partial x} + \frac{\partial \sigma_{xy}}{\partial y} = 0 \tag{2a}$$

$$\frac{\partial \sigma_{xy}}{\partial x} + \frac{\partial \sigma_{yy}}{\partial y} = 0, \tag{2b}$$

4

with the normal stresses σ_{xx} and σ_{yy} in x- and y-direction, respectively and the shear stress σ_{xy}. Adding the constitutive equations for linear elastic material behavior

$$\epsilon_{xx}^{el} = \frac{1}{E}\left(\sigma_{xx} - \nu\sigma_{yy}\right), \tag{3a}$$

$$\epsilon_{yy}^{el} = \frac{1}{E}\left(\sigma_{yy} - \nu\sigma_{xx}\right), \tag{3b}$$

and

$$\epsilon_{xy}^{el} = \frac{1}{2G}\sigma_{xy}, \tag{3c}$$

with the Young's modulus E, the shear modulus G, and the Poisson's ratio ν leads to the elastic strains ϵ_{xx}^{el}, ϵ_{yy}^{el}, and ϵ_{xy}^{el}.

These elastic strains have to be added to the plastic strains ϵ_{xx}^{pl}, ϵ_{yy}^{pl} and ϵ_{xy}^{pl} that are induced during the rolling process. Hence, the total strains read as

$$\epsilon_\Lambda = \epsilon_\Lambda^{el} + \epsilon_\Lambda^{pl}, \quad \Lambda \in \{xx, xy, yy\}. \tag{4}$$

The displacement fields $u = u(x,y)$ and $v = v(x,y)$ in longitudinal and lateral direction are linked with the strains by

$$\epsilon_{xx} = \frac{\partial u}{\partial x} \tag{5a}$$

and

$$\epsilon_{yy} = \frac{\partial v}{\partial y} \tag{5b}$$

and the shear strain γ_{xy} is defined as

$$\gamma_{xy} = 2\epsilon_{xy} = \frac{\partial u}{\partial y} + \frac{\partial v}{\partial x}. \tag{6}$$

Furthermore, the three unknown strain components are subject to the compatibility equation

$$\frac{\partial^2 \epsilon_{xx}}{\partial y^2} + \frac{\partial^2 \epsilon_{yy}}{\partial x^2} = \frac{\partial^2 \gamma_{xy}}{\partial x \partial y} \tag{7}$$

to obtain continuous, single-valued displacements (cf. [17]). Inserting Hooke's law (3) into the relations (4) and further into the compatibility equation (7) yields

$$\frac{\partial^2}{\partial y^2}\left[\frac{1}{E}\left(\sigma_{xx} - \nu\sigma_{yy}\right)\right] + \frac{\partial^2}{\partial x^2}\left[\frac{1}{E}\left(\sigma_{yy} - \nu\sigma_{xx}\right)\right]$$
$$-\frac{\partial^2}{\partial x \partial y}\left(\frac{1}{G}\sigma_{xy}\right) = -\frac{\partial^2 \epsilon_{xx}^{pl}}{\partial y^2} - \frac{\partial^2 \epsilon_{yy}^{pl}}{\partial x^2} + 2\frac{\partial^2 \epsilon_{xy}^{pl}}{\partial x \partial y}. \tag{8}$$

Summing up the derivatives of (2a) and (2b) with respect to x and y, respectively, gives

$$\frac{\partial^2 \sigma_{xy}}{\partial x \partial y} = -\frac{1}{2}\left(\frac{\partial^2 \sigma_{xx}}{\partial x^2} + \frac{\partial^2 \sigma_{yy}}{\partial y^2}\right).$$

5

This expression helps to eliminate the shear stress and Poisson's ratio from (8) using $G = \frac{E}{2(1+\nu)}$ and $E = \text{const}$. The simplified version of (8) thus reads as

$$\frac{\partial^2 \sigma_{xx}}{\partial x^2} + \frac{\partial^2 \sigma_{xx}}{\partial y^2} + \frac{\partial^2 \sigma_{yy}}{\partial x^2} + \frac{\partial^2 \sigma_{yy}}{\partial y^2}$$
$$= -E \left(\frac{\partial^2 \epsilon_{xx}^{pl}}{\partial y^2} + \frac{\partial^2 \epsilon_{yy}^{pl}}{\partial x^2} - 2\frac{\partial^2 \epsilon_{xy}^{pl}}{\partial x \partial y} \right). \tag{9}$$

As mentioned in [18], (9) shows that only plastic deformations with nonvanishing second derivatives induce residual stresses. That is, using a Taylor series expansion, constant and linear terms would not induce additional elastic deformations. This is because the right hand side of (9) vanishes for such terms resulting in the trivial solution $\sigma_{xx} = \sigma_{yy} = \sigma_{xy} = 0$ for the considered case of absent surface tractions at the boundary of the plate.

An effective way to deal with the two-dimensional problem (9) was introduced by [19]. The so called *Airy's stress function* $F = F(x, y)$, which satisfies

$$\sigma_{xx} = \frac{\partial^2 F}{\partial y^2}, \quad \sigma_{yy} = \frac{\partial^2 F}{\partial x^2}, \quad \sigma_{xy} = -\frac{\partial^2 F}{\partial x \partial y}, \tag{10}$$

can be inserted into (9) to obtain the fourth order inhomogeneous partial differential equation

$$\Delta\Delta F = \underbrace{-E \left(\frac{\partial^2 \epsilon_{xx}^{pl}}{\partial y^2} + \frac{\partial^2 \epsilon_{yy}^{pl}}{\partial x^2} - 2\frac{\partial^2 \epsilon_{xy}^{pl}}{\partial x \partial y} \right)}_{f(x,y)}, \tag{11}$$

with the Laplacian $\Delta = \frac{\partial^2}{\partial x^2} + \frac{\partial^2}{\partial y^2}$. Eq. (11) is also known as extended biharmonic equation. The term *extended* hints at the inhomogeneous disturbance term on the right hand side. In the absence of plastic strains, (11) is called biharmonic equation. Because of (11), the compatibility equation (7) is automatically fulfilled by the chosen ansatz (10). Another interesting feature of the (extended) biharmonic equation is its independence of the Poisson's ratio ν.

Instead of solving the initial partial differential equation for the unknown stresses, strains and displacements subject to the compatibility equation (7), it is equivalent to solve (11) for the stress function F. Once F is known, the stresses are calculated based on (10) and the elastic strains follow from (3).

It remains to determine the displacements by integrating the strains to

$$u(x, y) = \int_0^x \epsilon_{xx}^{el}(\bar{x}, y) \mathrm{d}\bar{x} + \int_0^x \epsilon_{xx}^{pl}(\bar{x}, y) \mathrm{d}\bar{x} + \frac{1}{E}\phi(y) \tag{12a}$$

and

$$v(x, y) = \int_0^y \epsilon_{yy}^{el}(x, \bar{y}) \mathrm{d}\bar{y} + \int_0^y \epsilon_{yy}^{pl}(x, \bar{y}) \mathrm{d}\bar{y} + \frac{1}{E}\psi(x), \tag{12b}$$

with scalar functions $\phi(y)$ and $\psi(x)$. They define the boundary values of the displacements and cannot be chosen arbitrarily. Note that (12) satisfies the displacement-strain relations (5) regardless of the choice of $\phi(y)$ and $\psi(x)$.

Combination of (6), (4), and (3c) yields

$$\gamma_{xy} = \frac{\partial u}{\partial y} + \frac{\partial v}{\partial x} = 2\epsilon_{xy}^{el} + 2\epsilon_{xy}^{pl} = \frac{2(1+\nu)}{E}\sigma_{xy} + 2\epsilon_{xy}^{pl}$$

6

and, by inserting (12), it follows that

$$2E\epsilon_{xy}^{pl} + 2(1+\nu)\sigma_{xy}$$

$$= E\int_0^x \frac{\partial \epsilon_{xx}^{el}(\bar{x},y)}{\partial y}\mathrm{d}\bar{x} + E\int_0^x \frac{\partial \epsilon_{xx}^{pl}(\bar{x},y)}{\partial y}\mathrm{d}\bar{x} + \frac{\mathrm{d}\phi(y)}{\mathrm{d}y}$$

$$+ E\int_0^y \frac{\partial \epsilon_{yy}^{el}(x,\bar{y})}{\partial x}\mathrm{d}\bar{y} + E\int_0^y \frac{\partial \epsilon_{yy}^{pl}(x,\bar{y})}{\partial x}\mathrm{d}\bar{y} + \frac{\mathrm{d}\psi(x)}{\mathrm{d}x}.$$

Furthermore, using (3a), (3b), and the definition (10) yields

$$\frac{\mathrm{d}\psi(x)}{\mathrm{d}x} + \frac{\mathrm{d}\phi(y)}{\mathrm{d}y}$$

$$= 2E\epsilon_{xy}^{pl} - 2(1+\nu)\frac{\partial^2 F}{\partial x\partial y}$$

$$- \int_0^x \left(\frac{\partial^3 F(\bar{x},y)}{\partial y^3} - \nu\frac{\partial^3 F(\bar{x},y)}{\partial \bar{x}^2\partial y}\right)\mathrm{d}\bar{x}$$

$$- \int_0^y \left(\frac{\partial^3 F(x,\bar{y})}{\partial x^3} - \nu\frac{\partial^3 F(x,\bar{y})}{\partial x\partial \bar{y}^2}\right)\mathrm{d}\bar{y}$$

$$- E\left(\int_0^x \frac{\partial \epsilon_{xx}^{pl}(\bar{x},y)}{\partial y}\mathrm{d}\bar{x} + \int_0^y \frac{\partial \epsilon_{yy}^{pl}(x,\bar{y})}{\partial x}\mathrm{d}\bar{y}\right)$$

$$= \delta_1(x) + \delta_2(y). \tag{13}$$

The left-hand side of (13) splits up in a term $\delta_1(x) = \frac{\mathrm{d}\psi(x)}{\mathrm{d}x}$ depending only on x and a term $\delta_2(y) = \frac{\mathrm{d}\phi(y)}{\mathrm{d}y}$ depending only on y. Integrating these terms gives

$$\psi(x) = \int_0^x \delta_1(\bar{x})\mathrm{d}\bar{x} + C_{\delta 1} \tag{14a}$$

and

$$\phi(y) = \int_0^y \delta_2(\bar{y})\mathrm{d}\bar{y} + C_{\delta 2}, \tag{14b}$$

with integration constants $C_{\delta 1}$ and $C_{\delta 2}$ representing the translational degrees of freedom of the rigid body motion of the plate. Equation (14) delivers insight into the limitations of choosing the functions $\psi(x)$ and $\phi(y)$.

2.1.2. Derivation of the boundary conditions

Besides fulfilling the biharmonic equation (11), a suitable stress function F has to satisfy certain boundary conditions. Two different types of boundary conditions can be identified: one giving a restriction on the displacements at the boundary and one constraining the stresses at the boundary. Only the latter one is discussed because the first one (rigid body motion) is not relevant in the considered problem.

The stresses at the boundary Γ of the plate (cf. Fig. 3) may be expressed by the components of the external stress vector $T_x^n = T_x^n(s)$ in longitudinal and $T_y^n = T_y^n(s)$ in lateral direction, depending on the curvilinear coordinate s. They are defined by

$$T_x^n = \sigma_{xx}n_x + \sigma_{xy}n_y \tag{15a}$$

and

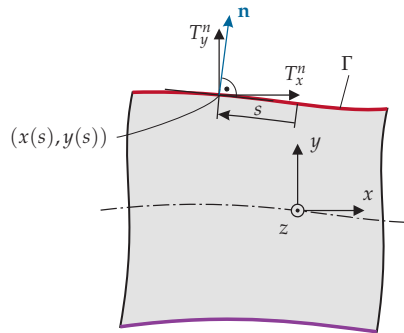$$T_y^n = \sigma_{xy}n_x + \sigma_{yy}n_y. \tag{15b}$$

7

Figure 3: Boundary conditions at the plate contour.

Here, n_x and n_y denote the components of the unit normal vector

$$\mathbf{n} = \begin{bmatrix} n_x \\ n_y \end{bmatrix} = \begin{bmatrix} \frac{\mathrm{d}y}{\mathrm{d}s} \\ -\frac{\mathrm{d}x}{\mathrm{d}s} \end{bmatrix} \tag{16}$$

of the boundary Γ. The vector $\mathbf{n}$ points outwards. A specific point on the boundary Γ is defined by its Cartesian coordinates $(x(s), y(s))$. Insertion of (10) and (16) into (15) yields

$$T_x^n = \frac{\partial^2 F}{\partial y^2}\frac{\mathrm{d}y}{\mathrm{d}s} + \frac{\partial^2 F}{\partial x \partial y}\frac{\mathrm{d}x}{\mathrm{d}s} \tag{17a}$$

and

$$T_y^n = -\frac{\partial^2 F}{\partial x \partial y}\frac{\mathrm{d}y}{\mathrm{d}s} - \frac{\partial^2 F}{\partial x^2}\frac{\mathrm{d}x}{\mathrm{d}s}. \tag{17b}$$

In the considered problem, surface tractions are absent, i.e. the boundary conditions are $T_x^n = T_y^n = 0$.

2.2. Solution of the biharmonic equation

Searching for an exact solution of (11) and (17) is difficult. Only for trivial shapes, specific plastic deformations and particular boundary conditions, exact solutions may be obtained. To circumvent this difficulty, an approximate solution with a stress function that automatically satisfies (11) but not necessarily (17) is used.

2.2.1. Power series solutions

The solution F_{hom} of the associated homogeneous biharmonic equation

$$\frac{\partial^4 F_{hom}}{\partial x^4} + 2\frac{\partial^4 F_{hom}}{\partial x^2 \partial y^2} + \frac{\partial^4 F_{hom}}{\partial y^4} = 0 \tag{18}$$

and the particular solution F_{part} of the extended biharmonic equation (11) are added to form the solution

$$F = F_{hom} + F_{part}. \tag{19}$$

This superposition approach is possible due to the linearity of (11). F_{part} fulfills (11), but not necessarily (17). Therefore, F_{hom}, which is independent of the plastic deformation (cf. (18)), is chosen so that F satisfies (17). In this work, power series are used to approximate F_{part}. A method originally proposed by [20] is applied to obtain the power series.

8

A single homogeneous solution term Ψ_i with degree p is characterized by

$$\Psi_i = \sum_{j=0}^{p} \sum_{k=0}^{p} b_{j,k} x^j y^k \tag{20}$$

with some constants $b_{j,k}$. They are chosen so that the homogeneous biharmonic equation (18) is individually satisfied by each term Ψ_i. By insertion of Ψ_i into (18), a system of linear equations for determining the unknown coefficients $b_{j,k}$ is obtained. F_{hom} is a linear combination of the terms Ψ_i, i.e.,

$$F_{hom} = \sum_{i=1}^{n} a_i \Psi_i = \mathbf{J}^{\mathrm{T}} \mathbf{a} \tag{21}$$

with $\mathbf{a} = [a_i]_{i=1,\dots,n}$ and $\mathbf{J} = [\Psi_i]_{i=1,\dots,n}$ for some constants a_i, $i = 1, \dots, n$. The coefficients a_i will be used satisfy the boundary conditions. In an analogous manner, a series solution for the extended biharmonic equation (11) can be found if the plastic strains are approximated by a two-dimensional power series

$$\epsilon_\Lambda^{pl} = \sum_{i=0}^{k} \sum_{j=0}^{i} \underbrace{c_{\Lambda,\gamma} x^{i-j} y^j}_{\Phi_{\Lambda,\gamma}}, \quad \Lambda \in \{xx, xy, yy\} \tag{22}$$

with the degree k. The index function

$$\gamma = \frac{(i+1)i}{2} + j$$

defines an incrementing index γ for the elements of the double sum in (22). Each individual solution term $F_{part,\gamma}$ of the particular solution

$$F_{part} = \sum_{\gamma=0}^{n_{part}} F_{part,\gamma}$$

with $n_{part} = \frac{k^2}{2} + \frac{3}{2}k$ must satisfy (11), i.e.,

$$\Delta\Delta F_{part,\gamma} = \underbrace{-E\left(\frac{\partial^2 \Phi_{xx,\gamma}}{\partial y^2} + \frac{\partial^2 \Phi_{yy,\gamma}}{\partial x^2} - 2\frac{\partial^2 \Phi_{xy,\gamma}}{\partial x \partial y} \right)}_{f_\gamma(x,y)} \tag{23}$$

with $\Phi_{\Lambda,\gamma}$ according to (22). Similar to (20), $F_{part,\gamma}$ is based on a two-dimensional polynomial

$$F_{part,\gamma}(x,y) = \sum_{j=0}^{\bar{p}} \sum_{k=0}^{\bar{p}} \bar{b}_{j,k} x^j y^k,$$

with the degree $\bar{p}$ selected properly depending on the degree of $f_\gamma(x,y)$. The polynomial coefficients $\bar{b}_{j,k}$ are found from a comparison of coefficients in (23).

As mentioned earlier, a solution that satisfies the boundary conditions in an approximate manner is derived. Inserting an approximate ansatz $\hat{F}$ for Airy's stress function into the boundary conditions (17) gives the residuals

$$\mathcal{R}_x(\hat{F}) = \frac{\partial^2 \hat{F}}{\partial y^2} \frac{\mathrm{d}y}{\mathrm{d}s} + \frac{\partial^2 \hat{F}}{\partial x \partial y} \frac{\mathrm{d}x}{\mathrm{d}s} \neq 0$$

9

and

$$\mathcal{R}_y(\hat{F}) = -\frac{\partial^2 \hat{F}}{\partial x \partial y}\frac{\mathrm{d}y}{\mathrm{d}s} - \frac{\partial^2 \hat{F}}{\partial x^2}\frac{\mathrm{d}x}{\mathrm{d}s} \neq 0.$$

The idea is that these residuals vanish in a weighted integral sense, i.e.,

$$\int_\Gamma v_x \mathcal{R}_x(\hat{F})\mathrm{d}s + \int_\Gamma v_y \mathcal{R}_y(\hat{F})\mathrm{d}s = 0, \tag{24}$$

with the weighting functions v_x and v_y. Two different weighting functions are necessary to avoid that only the sum $\mathcal{R}_x(\hat{F}) + \mathcal{R}_y(\hat{F})$ vanishes. With $\hat{F} = \hat{F}_{hom} + \hat{F}_{part}$ and $\hat{F}_{hom} = \hat{\mathbf{j}}^\mathrm{T}\mathbf{a}$ according to (19) and (21) the residual terms can be written as

$$\mathcal{R}_x(\hat{F}) = \left(\frac{\partial^2 \hat{\mathbf{j}}^\mathrm{T}}{\partial y^2}\frac{\mathrm{d}y}{\mathrm{d}s} + \frac{\partial^2 \hat{\mathbf{j}}^\mathrm{T}}{\partial x \partial y}\frac{\mathrm{d}x}{\mathrm{d}s}\right)\mathbf{a} + \frac{\partial^2 \hat{F}_{part}}{\partial y^2}\frac{\mathrm{d}y}{\mathrm{d}s}$$
$$+ \frac{\partial^2 \hat{F}_{part}}{\partial x \partial y}\frac{\mathrm{d}x}{\mathrm{d}s}$$

and

$$\mathcal{R}_y(\hat{F}) = \left(-\frac{\partial^2 \hat{\mathbf{j}}^\mathrm{T}}{\partial x \partial y}\frac{\mathrm{d}y}{\mathrm{d}s} - \frac{\partial^2 \hat{\mathbf{j}}^\mathrm{T}}{\partial x^2}\frac{\mathrm{d}x}{\mathrm{d}s}\right)\mathbf{a} - \frac{\partial^2 \hat{F}_{part}}{\partial x \partial y}\frac{\mathrm{d}y}{\mathrm{d}s}$$
$$- \frac{\partial^2 \hat{F}_{part}}{\partial x^2}\frac{\mathrm{d}x}{\mathrm{d}s}.$$

Now a slightly modified least-squares method as reported by [21] is employed. The method suggests using the residuals $\mathcal{R}_x(\Psi_i)$ and $\mathcal{R}_y(\Psi_i)$ as weighting functions v_x and v_y, respectively. Other weighting functions are also suitable for the given problem, but $\mathcal{R}_x(\Psi_i)$ and $\mathcal{R}_y(\Psi_i)$ simplify the evaluation of the integrals in (24). Equation (24) must vanish individually for each pair of weighting functions $v_x = \mathcal{R}_x(\Psi_i)$ and $v_y = \mathcal{R}_y(\Psi_i)$. This results in a system of linear equations

$$\left(\mathbf{A}_x + \mathbf{A}_y\right)\mathbf{a} = \mathbf{y}_x + \mathbf{y}_y \tag{25}$$

with the matrices

$$\mathbf{A}_x = \int_\Gamma \mathcal{R}_x(\hat{\mathbf{j}})\mathcal{R}_x(\hat{\mathbf{j}}^\mathrm{T})\mathrm{d}s \tag{26a}$$

$$\mathbf{A}_y = \int_\Gamma \mathcal{R}_y(\hat{\mathbf{j}})\mathcal{R}_y(\hat{\mathbf{j}}^\mathrm{T})\mathrm{d}s \tag{26b}$$

and the vectors

$$\mathbf{y}_x = -\int_\Gamma \mathcal{R}_x(\hat{\mathbf{j}})\mathcal{R}_x(\hat{F}_{part})\mathrm{d}s \tag{27a}$$

$$\mathbf{y}_y = -\int_\Gamma \mathcal{R}_y(\hat{\mathbf{j}})\mathcal{R}_y(\hat{F}_{part})\mathrm{d}s. \tag{27b}$$

The residual of a vector is just an assembly of the residuals of its components. The fact that the proposed method generates symmetric matrices $\mathbf{A}_x$ and $\mathbf{A}_y$ can be utilized when solving (25) for the unknown coefficients a_i. The numerical properties of $\mathbf{A}_x$ and $\mathbf{A}_y$ are of good nature, even for polynomial approximations with high degrees. For simplicity reasons, henceforth the approximate solution $\hat{F}$ is no longer denoted with a hat.

10

2.2.2. Parameterization of the plate contour

There exist various methods to deal with curvilinear boundary domains of differential equations. In some cases, a change of the chosen coordinate system may lead to a formally simpler representation of the boundary. Polar coordinates, for instance, should be used for circular computational domains.

The problem considered in this work requires a tailored definition of the boundary, which also allows to track the camber during several rolling passes. A closed-form parametric representation of the boundary seems favorable in terms of integration along the edges. As indicated in Fig. 4, a convenient formulation consists of four polynomials representing the four boundaries.
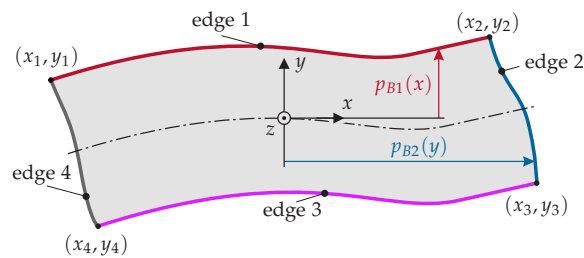

Figure 4: Definition of edges for a plate with a curvilinear boundary.

A point on the edges 1 and 3 (lateral edges) is parameterized by a polynomial with degree N_B as

$$p_{Bj}(x) = \sum_{i=0}^{N_B} d_{j,i} x^i, \quad j = 1, 3 \tag{28}$$

and on the edges 2 and 4 (head and tail) as

$$p_{Bj}(y) = \sum_{i=0}^{N_B} d_{j,i} y^i, \quad j = 2, 4. \tag{29}$$

Hence, the curvilinear boundary Γ is described by

$$\Gamma = \begin{cases} \text{edge } 1 = \left\{ (x,y) \middle| x \in [x_1, x_2], y = p_{B1}(x) \right\} \\ \text{edge } 2 = \left\{ (x,y) \middle| y \in [y_3, y_2], x = p_{B2}(y) \right\} \\ \text{edge } 3 = \left\{ (x,y) \middle| x \in [x_4, x_3], y = p_{B3}(x) \right\} \\ \text{edge } 4 = \left\{ (x,y) \middle| y \in [y_4, y_1], x = p_{B4}(y) \right\}. \end{cases}$$

Due to the integration along a curved boundary Γ, e.g. in (24), it seems reasonable to introduce a curvilinear coordinate s defined by

$$\mathrm{d}s = \sqrt{1 + \left(\frac{\mathrm{d}p_{Bj}(x)}{\mathrm{d}x} \right)^2} \, \mathrm{d}x$$

for $j \in \{1, 3\}$ and

$$\mathrm{d}s = \sqrt{1 + \left(\frac{\mathrm{d}p_{Bj}(y)}{\mathrm{d}y} \right)^2} \, \mathrm{d}y$$

for $j \in \{2, 4\}$.

11

A curved shape Γ generally precludes an analytical integration of (24). Therefore, the integrals are numerically evaluated by using a Gaussian quadrature.

An integral is thus approximated by a weighted sum

$$\int_{-1}^{1} f(\xi)\mathrm{d}\xi \approx \sum_{i=1}^{N} w_i f(\xi_i), \tag{30}$$

where N denotes the quadrature order and w_i represents the weight for the function value $f(\xi_i)$ at the sampling point ξ_i. Krylov (cf. [22]) showed that the sampling points of one possible quadrature method may be found as the roots of the Legendre polynomial

$$p_N(x) = \frac{1}{2^N N!} \frac{\mathrm{d}^N}{\mathrm{d}x^N}\left[\left(x^2 - 1\right)^N\right]$$

and that the corresponding weights are defined by

$$w_i = \int_{-1}^{1} \prod_{\substack{k=0 \\ k \neq i}}^{N} \frac{x - x_k}{x_i - x_k} \mathrm{d}x\,.$$

Additionally, a transformation

$$\int_{x_{low}}^{x_{upp}} f(x)\mathrm{d}x = \frac{x_{upp} - x_{low}}{2} \int_{-1}^{1} f(\xi)\mathrm{d}\xi$$

with

$$x = \frac{x_{upp} + x_{low}}{2} + \frac{x_{upp} - x_{low}}{2}\xi$$

and proper chosen integration boundaries x_{low} and x_{upp} (cf. Fig. 4) has to be performed. This transformation accounts for the different integration boundaries in (26) and (27) compared to (30).

2.2.3. Implementation

The simulation model is implemented in MATLAB 2012b using the linear algebra packages LAPACK and BLAS for matrix operations and for solving the linear system of equations (25). Furthermore, the numerical integration is performed in C-functions to achieve low computation times. The necessary computations to achieve the plate contour are shown in Fig. 5. The procedure starts with an initial plate contour achieved from measurements. In every calculation step, the contour has to be approximated by the polynomial representation (28) and (29). Furthermore, the plastic strain (1) is estimated according to (22). Afterwards the system of linear equations (25) is set up and solved for the coefficient vector $\mathbf{a}$. Finally, the plate contour results from the displacements (12)-(14) at the boundary Γ of the plate.

3. Simulation results

In the following, simulation results are compared to measurement results for a typical plate rolled at AG der Dillinger Hüttenwerke, Germany.

The considered plate is rolled out from an initial plate thickness of 87 mm to its final thickness 36.5 mm using 11 rolling passes. As inputs for the computations, the input thickness and the exit thickness of the plate at the entry and exit of the rolling gap, respectively, are used. This thickness profiles are obtained from measurements. Only plastic deformation along the direction x is considered, hence the plastic deformations ϵ_{yy}^{pl} and ϵ_{xy}^{pl} vanish. Moreover, the temperature is assumed to be uniform and the parameters used for the computations are listed in Tab. 1.

12

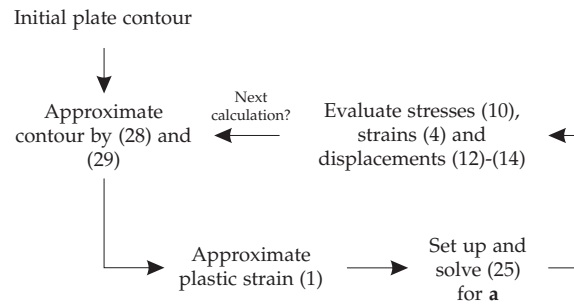Initial plate contour

Approximate contour by (28) and (29) ← Next calculation? ← Evaluate stresses (10), strains (4) and displacements (12)-(14)

Approximate plastic strain (1) → Set up and solve (25) for **a**

Figure 5: Computational scheme for the estimation of the plate contour.

Table 1: Parameters used for the computations.

Parameter	Value	Unit
E	140	kN/mm^2
ν	0.3	
n	70	
k	8	
p	19	
n_{part}	44	
N_B	4	
N	20	

Measurement data is only available before and after the rolling passes 1, 3, 5 and 11. Therefore, the calculation is done in three steps, each covering several rolling passes, as indicated in Fig. 6. The simulation uses measurement data only for the initial contour before calculation step I. In case of the remaining initial contours for the calculation steps II and III, the resulting contour from the preceding calculation step is used.

For the three calculation steps, Fig. 7 shows the plastic strains ϵ_{xx}^{pl} approximated by polynomials of degree $k = 8$. The real plate contour is measured by means of a laser line scanner and some image processing algorithms. The scanner is arranged across the roller table. It captures images (1D arrays) as the plate moves along the roller table. Its images are joined by software to generate a full 2D picture of the plate contour. Due to the purely translational motion of the plate this is a consecutive arrangement of 1D arrays. This strategy gives a relatively low image resolution along the direction x, which does not allow an accurate measurement of the edges 2 and 4 (head and tail of the plate). However, this is not a problem because mainly the edges 1 and 3 (lateral edges) are relevant for the development of camber. Consequently, only the edges 1 and 3 are shown and analyzed in the following. Fig. 8 depicts the simulated and measured plate contours for all three calculation steps. Despite the fact that the calculation covers 10 rolling passes, the model mismatch is in an acceptable range. More accurate results would be achieved if the model were fed with measurement data not only at the beginning but after each rolling pass with measurements.

Fig. 9 shows the residual stresses σ_{xx} after the first calculation step. It indicates that the homogeneous stress boundary conditions at the head and the tail end of the plate are nicely satisfied. The simulation was carried out on a personal computer with an i7-2600 processor featuring 3.4 GHz and 16 GB of RAM. With this hardware configuration, a rolling pass can be simulated within less than 1 ms CPU time.
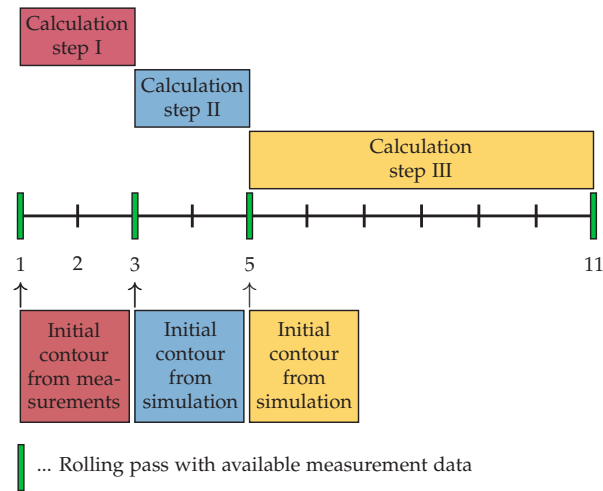
13

Figure 6: Explanation of the three calculation steps.

4. Analysis of the reasons for the generation of camber

As shown in the last section, the proposed model is able to precisely predict the generation of camber with known profiles of the input and output thickness of the plate. So it is obvious to use the mathematical model to analyze the reasons for the generation of camber. One reason is the presence of an asymmetric input thickness in the lateral direction.

Therefore, the last rolling pass of a plate with the final plate dimensions $l = 40$ m and $b = 2$ m and the final plate thickness $h_{out}(x, y) = \bar{h}_{out} = 8$ mm is considered. A rectangular shape of the plate before the rolling pass is presumed and the parameters are taken from Tab. 1. The relatively long and thin plate was chosen, because from experience exactly this type of plates is more likely to camber.

For simplicity, the input profile $h_{in}(x, y)$ is assumed to be affine in the y-direction and constant in the x-direction. It is therefore parameterized in the form

$$h_{in}(x, y) = \bar{h}_{in} + \frac{y}{b} \Delta h_{in},$$

with the mean input thickness $\bar{h}_{in}$ and the lateral asymmetry of the input thickness Δh_{in}. Furthermore, an average thickness reduction of $\frac{\bar{h}_{in}}{\bar{h}_{out}} - 1 = 8\%$ during the pass is assumed. The chosen input and output thickness profiles induce no residual stresses because in this case the right-hand side of (9) vanishes. Moreover, the resulting contour of the plate is symmetrical with respect to the y-axis. As a measure of the resulting camber, the lateral deviation v_{max} of the intersection of edge 2 and edge 3 (cf. Fig. 10) is used.

In Fig. 11, v_{max} is shown for different input asymmetries Δh_{in}, indicating an almost linear dependence between those two quantities. In particular, Fig. 11 shows that asymmetries of about 3 hundredths of a millimeter result in deviations of more than half a meter.

Hence, a precise control of the asymmetry of the thickness of the plate in the range of a few hundredths of a millimeter is required to prevent the plate from camber. Further analysis for the reasons of camber, e.g., differences in the deformation resistance of the plate or asymmetric conditions of the mechanical setup of the mill in the lateral direction, necessitates the knowledge of a suitable model for the formation of the rolling gap, see, e.g., [23].
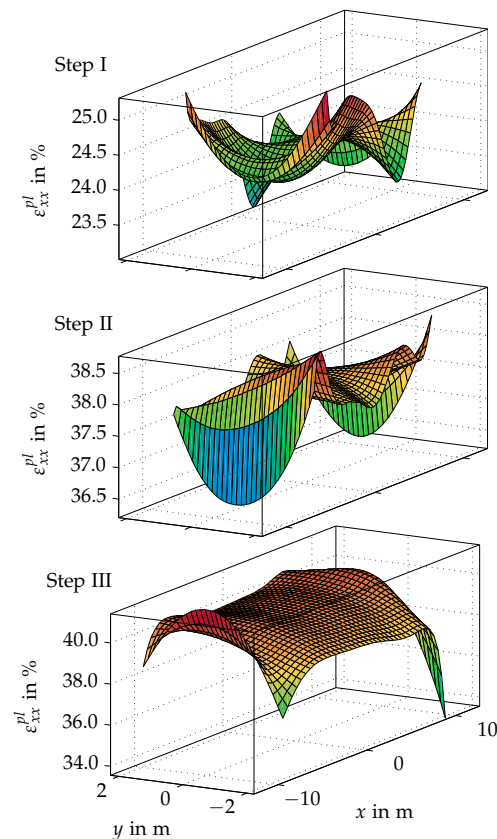
14

Figure 7: Plastic strains $\epsilon_{xx}^{pl}(x,y)$ for the three calculation steps.

5. Conclusion and outlook

A continuum mechanics model for the contour evolution of plates in hot rolling was presented. The input and output thickness profile of the plate and the initial contour of the plate serve as inputs of the model. The total strains of the two-dimensional model result from a superposition of elastic and plastic strains. The usage of linear elasticity leads to a model consisting of the so called extended biharmonic equation. This partial differential equation is solved by using a power series ansatz. A weighted residuals approach is employed to fulfill the homogeneous boundary conditions. Finally, the model was validated by means of a measured evolution of the plate contour. The tractable model shows a good agreement with the measured contour geometries and requires only a low computational effort. Moreover, reasons for the generation of camber were analyzed by means of the presented model. This analysis shows that a precise control of the thickness profile in the lateral direction is necessary to prevent camber.

The developed model, together with an appropriate model for the formation of the rolling gap, serves as a basis to analyze other possible reasons for the generation of camber and to identify improvements of the mechanical setup of the mill to optimize the evolution of the plate contour. Together with a suitable contour measurement device, the model will be exploited to curb the formation of camber by tailored optimization based feedback control concepts, see, e.g., [11]. They aim at minimizing the deviation between a desired and the achieved contour of the plate in terms of a desired cost function. To this end, an asymmetric adjustment of the rolling gap actuators may be used as control input. Additional cost function terms, e.g. penalizing the rate of change of the mill stand tilt, enable an intuitive adjustment of the closed loop behavior. Furthermore, optimization based control facilitates the systematic incorporation
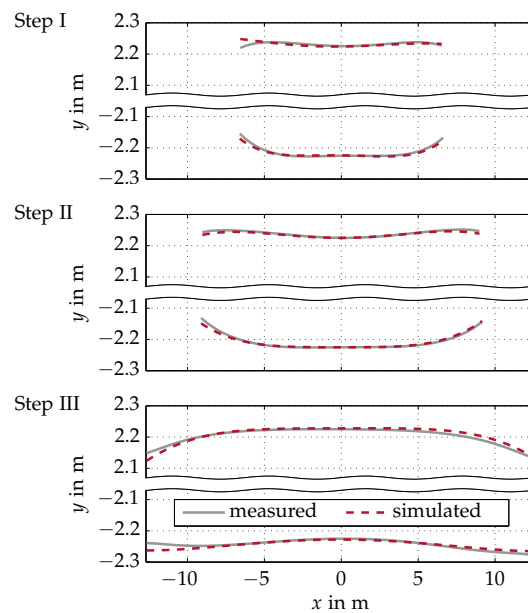
15

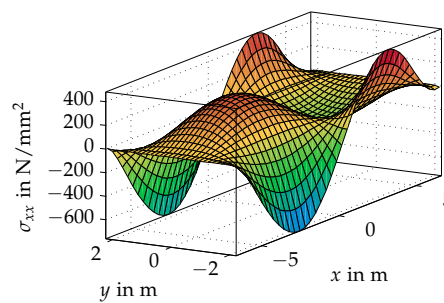Figure 8: Simulated and measured contour evolution for the three calculation steps.

Figure 9: Normal stress distribution σ_{xx} after calculation step I.

of input and state constraints. Hence, limits for the roll gap asymmetry may be considered in the control law. As the contour of the final plate influences the quality and the usable area of the plate, reduced camber leads to an increased yield of the final product.

Acknowledgements

References

[1] M. Abbaspour, A. Saboonchi, Work roll thermal expansion control in hot strip mill, Appl. Math. Modell. 32 (2008) 2652–2669.
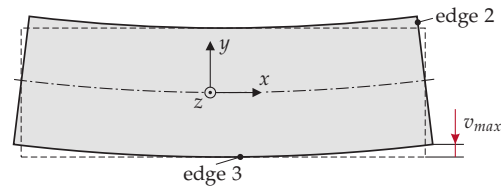
16

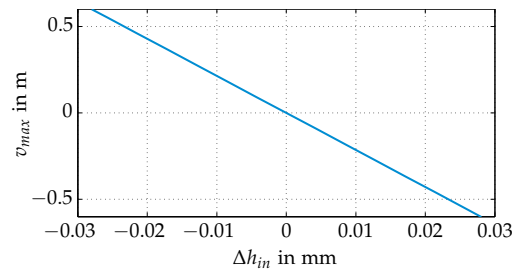Figure 10: Maximum deviation of the plate in the lateral direction v_{max}.

Figure 11: Maximum deviation in the lateral direction v_{max} as a function of the asymmetry of the input thickness Δh_{in}.

[2] X. Wang, F. Li, Q. Yang, A. He, FEM analysis for residual stress prediction in hot rolled steel strip during the run-out table cooling, Appl. Math. Modell. 37 (2013) 586–609.

[3] T. Ishikawa, Y. Tozawa, J. Nishizawa, Fundamental study on snaking in strip rolling, Transactions of the Iron and Steel Inst. of Jpn. 28 (6) (1988) 485–490.

[4] T. Shiraishi, H. Ibata, A. Mizuta, S. Nomura, E. Yoneda, K. Hirata, Relation between camber and wedge in flat rolling under restrictions of lateral movement, Transactions of the Iron and Steel Inst. of Jpn. 31 (6) (1991) 583–587.

[5] A. Dixon, D. Yuen, Mathematical analysis of the effects of width-wise asymmetric rolling conditions on head-end wedge, camber and off-centre, Rolling 2013 - 9th Int. Rolling Conf. and the 6th European Rolling Conf., Venice, Italy, 2013.

[6] Y. Tanaka, K. Omori, T. Miyake, K. Nishizaki, M. Inoue, S. Tezuka, Camber control techniques in plate rolling, Tech. Rep. 16, Kawasaki Steel (1987).

[7] Y. Okamura, I. Hoshino, State feedback control of the strip steering for aluminum hot rolling mills, Control Eng. Pract. 5 (8) (1997) 1035–1042.

[8] T. Kiyota, H. Matsumoto, Y. Adachi, E. Kondo, Y. Tsuji, S. Aso, Tail crash control in hot strip mill by LQR, Proc. of the am. Control Conf., Denver, Colorado, USA, 2003, pp. 3049–3054.

[9] M. Okada, K. Murayama, Y. Anabuki, Y. Hayashi, VSS control of strip steering for hot rolling mills, Proc. of the 16th IFAC World Congr., Prague, Czech Republic, 2005, pp. 1681–1686.

[10] A. Ollikkala, T. Kananen, A. Mäkynen, M. Holappa, E. Torppa, T. Harvala, A single camera system for camber measurement in hot strip rolling, Rolling 2013 - 9th International Rolling Conference and the 6th European Rolling Conference, Venice, Italy, 2013.

[11] I. Choi, J. Rossiter, J. Chung, P. Fleming, An MPC strategy for hot rolling mills and applications to strip threading control problems, Proc. of the 17th IFAC World Congr., Seoul, Korea, 2008, pp. 1661–1662.

[12] Y. Kang, Y. J. Choi, G. Oh, S. Won, Estimation of camber generation in rough rolling process, IFAC MMM 2013 Int. Symposium, San Diego, USA, 2013, pp. 436–439.

[13] D. L. Biggs, S. J. Hardy, K. J. Brown, Finite element modelling of camber development during hot rolling of strip steel, Vol. 25 of Ironmak. and Steelmak., 1998, pp. 81–89.

[14] A. Nilsson, FE simulations of camber in hot strip rolling, J. of Mater. Proc. Tech. (80–81) (1998) 325–329.

[15] M. Trull, D. McDonald, A. Richardson, D. C. J. Farrugia, Advanced finite element modelling of plate rolling operations, J. of Mater. Proc. Tech. 177 (2006) 513–516.

[16] J. H. Ruan, L. W. Zhang, S. D. Gu, W. B. He, S. H. Chen, 3D FE modelling of plate shape during heavy plate rolling, Vol. 41 of Ironmak. and Steelmak., 2014, pp. 199–205.

[17] M. H. Sadd, Elasticity, Theory, Applications and Numerics, Academic Press, Burlington, 2009.

[18] H. Schimmöller, Analytische Behandlung von Eigenspannungszuständen auf der Grundlage der Elastizitätstheorie, PhD dissertation, Technische Universität Hamburg-Harburg, 1992.

[19] G. B. Airy, On the strains in the interior of beams, no. 153 in Philosophical transactions of the Royal Society of Lond., 1863, pp. 49–80.

[20] A. Pucher, Über die Berechnung der Einflußfelder ebener Platten, Berichte der Gesellschaft von Freunden der technischen Hochschule Berlin, 1940, p. 60.

17

[21] J. N. Reddy, An Introduction to the Finite Element Method, 3rd Edition, McGraw-Hill London, 2006.

[22] V. I. Krylov, Approximate calculation of integrals, MacMillan, London, 1962.

[23] T. König, A. Steinböck, A. Kugi, R. Heeg, T. Kiefer, Deflection and bending model of a four-high mill stand for heavy plate rolling, in: Proceedings of the 4th International Conference on Modelling and Simulation of Metallurgical Processes in Steelmaking, STEELSIM, METEC InSteelCon 2011, Düsseldorf, Germany, 2011.

18

The content of this post-print version is identical to the published paper but without the publisher's final layout or copy editing.